ORIGINAL ARTICLE

Synthesis and characterization of spark plasma sintered zirconia and ferrotitanium reinforced hybrid aluminium composite

Samuel Olukayode Akinwamide[1] · Mabontle Maleka[2] · Nthabiseng Motabeni[2] · Ojo Jeremiah Akinribide[2] · Falodun Eso Oluwasegun[3] · Peter Apata Olubambi[2]

Abstract

This research reports on the microstructural characterization and nanomechanical evaluation of hybrid aluminium-based composite, fabricated by reinforcing pure aluminium matrix with zirconia (ZrO_2) and ferrotitanium (TiFe) particles. The composites were consolidated using the spark plasma sintering technique, and the properties of the reinforced composites were examined and compared with pure aluminium samples fabricated using the same sintering parameters. The formation of new phases in the hybrid composites was ascertained using the X-ray diffraction technique, while the morphologies of the starting powders and as-sintered specimens were analysed using optical and scanning electron microscopes. Mechanical tests such as Vickers microhardness and frictional coefficient were determined to ascertain the respective strength and tribological performance. Nanoindentation test was also carried out to evaluate the nanomechanical properties such as penetration depth, elastic modulus, work indentation, and indentation creep. The results from this study revealed that mixing and sintering the admixed powders at sufficiently high temperature resulted in the formation of new phases which contributed to improved mechanical performance of the hybrid composites. The absence of pinning effect in loading and unloading curves from the nanoindentation test conducted confirmed the homogeneous dispersion of the reinforcement particles. Overall, the sample reinforced with 5% TiFe and 5% ZrO_2 exhibited the most improved mechanical properties, while the unreinforced aluminium sample recorded the least mechanical and nanomechanical performance.

1 Introduction

Nowadays, the use of aluminium in industries where improved engineering properties is of optimum importance is rapidly increasing. This has also paved the way for structural modification of this class of composites, leading to the invention of aluminium-based composites. Several researchers have investigated this novel class of composite,
and their findings have been documented in several studies [1, 2]. Some key properties of aluminium-based composites include cost-effectiveness, high strength-to-weight ratio, reduced density, and enhanced thermal conductivity [3–5].

Owing to the non-suitability of pure aluminium for structural application, it is essential to incorporate additional elements into the matrix of pure aluminium. Various researchers have utilized carbides, nitrides and agro-based materials for this purpose [6, 7]. At the same time, the dispersion of metallic ceramics into aluminium-based composites cannot be overemphasized, owing to the outstanding mechanical and wear-resistant properties they incorporate into the resulting composites. Hybrid metal matrix composites (HMMCs) are unique composites produced by the incorporation of two or more ceramic particles into the matrix of a metal. This class of advanced materials are known for their excellent wear resistance, light weight, low thermal expansion and high specific strength [8]. Owing to these excellent properties, HMMCs can be used in automotive and automobile

✉ Samuel Olukayode Akinwamide
samuel.akinwamide@aalto.fi;
akinwamidekayode@gmail.com

1 Advanced Manufacturing and Materials Research Group, Department of Mechanical Engineering, Espoo, Finland

2 Centre for Nanomechanics and Tribocorrosion, School of Mining Metallurgy and Chemical Engineering, University of Johannesburg, Johannesburg, South Africa

3 Department of Mechanical Engineering, Covenant University, Ota, Ogun State, Nigeria

engineering applications to manufacture parts such as piston rods, braking systems, brake discs, landing gear and shafts [9]. Several researchers have investigated on the reinforcement of aluminium matrix with different reinforcement particles via different primary processing routes with a focus on the microstructural and mechanical properties of the resulting aluminium-based composites. Also, the dispersion of two or more reinforcements often results in the agglomeration of the reinforcement particles [10]. Therefore, it is imperative to study how different reinforcement particles can be effectively dispersed in the aluminium matrix to eliminate possible agglomeration and fabricate HMMC with improved microstructural and nanomechanical properties.

Reinforcements such as silicon carbide, boron carbide, silicon nitride, and titanium carbide have been extensively utilized. Zirconia reinforcing mechanism includes its transformation from tetragonal phase (t-ZrO_2) to a highly distorted monoclinic phase (m-ZrO_2), which leads to a volume expansion of 3–5%, and reduction of compressive stress in the matrix material [11]. This ceramic reinforcement also increases the initial nucleation rate and strength in the metallic-based composite during compressive deformation [12]. Furthermore, TiFe (Ti: 45–70% and Fe: 10–30%) is known for its low density, excellent corrosion resistance and high strength at elevated temperatures [13]. They are produced from low-grade titanium ingot, which cannot be further subjected to recycling due to its oxidation degree.

Several processing techniques have been successfully adopted for the fabrication of aluminium-based composites. These include but are not limited to melt infiltration [14], casting [15], and powder metallurgy [16]. The latter technique is more advantageous as it eliminates the need to handle molten metal and promotes a better dispersion of reinforcement particles within the metallic matrix [17]. Among various powder metallurgy routes that have been explored, hot extrusion, hot pressing and pressureless sintering have remained prevalent. However, the spark plasma sintering (SPS) process has remained the least known metallic-based consolidating technique. The SPS method, a more recent approach, operates on the pressure-assisted pulsed energizing process to consolidate powder particles, thereby achieving enhanced densification [18, 19]. During the sintering process, rapid Joule heating combined with pulsed electrical discharge and high pressure provides rapid sintering kinetics for powders.

Since the properties of the resulting composite largely depend on the reinforcing particles, several investigations have been carried out to determine the influence of these particles on the overall properties of the composites. Akinwamide et al. [20] studied the effect of silicon carbide and ferrotitanium addition on aluminium-based composites. The specimens reinforced with only ferrotitanium exhibited reduced hardness compared to those reinforced with the addition of silicon carbide and ferrotitanium particles.

Jimtnez et al. [21] also reported on the microstructural and mechanical properties of aluminium composite reinforced with zirconia. The hardness values of the fabricated composites were reportedly increased upon the dispersion of different weight percentages of the zirconia reinforcement within the aluminium matrix. The influence of boron nitride and zirconia oxide on the mechanical properties of Al7075 hybrid composite was investigated by Kuldeep et al. [22]. Aside the reported homogeneous dispersion of the reinforcement particles within the aluminium alloy matrix, the ultimate tensile strength and hardness properties were also improved in the resulting hybrid composites. The reduced wear rate observed with increasing reinforcement also prevented material loss and ploughing from the sample surface.

The incorporation of second-phase particles has proven to be effective in enhancing the overall properties of aluminium-based composites, which has made them extensively used for various engineering applications [23, 24]. This present study investigates the morphological modification and mechanical properties of spark plasma sintered aluminium-based composites reinforced with particles of ZrO_2 and TiFe.

2 Experimental procedure

Different volume percentages of TiFe (average particle size: 176 μm, purity: 98.5%) and ZrO_2 (average particle size: 5 μm, purity: 99.5%) reinforcement powder particles were dispersed into the matrix of pure aluminium (average particle size: 25 μm, purity: 99.8%). The morphological features of the starting powders are shown in Fig. 1. The pure aluminium powder is seen to present different spherical, dense and smooth satellite particles, with the smaller satellites attaching to the bigger ones, as revealed in Fig. 1a. In contrast, the TiFe powder displayed in Fig. 1b shows a sharp-edged rock-like morphology. The microstructure of the ZrO_2 powder in Fig. 1c reveals a wide distribution of irregularly shaped agglomerated particles. The different composition of samples and their identification is presented in Table 1. To ensure homogenous distribution, the powders were mixed in a turbula mixer for a duration of 10 h. The ad-mixed powders were loaded into a die of size 40 mm, after which they were consolidated in an HHPD-25 model spark plasma sintering machine. Prior to sintering, a graphite sheet was placed between the powder and the die to prevent contamination and to ensure proper flow of current. The powders were consolidated at a temperature, heating rate, holding time and pressure of 520 ^{0}C, 100 ^{0}C/min, 5 min and 50 MPa, respectively. The samples were sectioned into smaller pieces for phase and metallographic examinations. The phase identification was conducted with a Rigaku Ultima IV X-ray diffraction machine with Cu-Kα radiation of 30 mA

Fig. 1 SEM micrographs of **a** pure aluminium, **b** ferrotitanium, and **c** zirconia staring powders

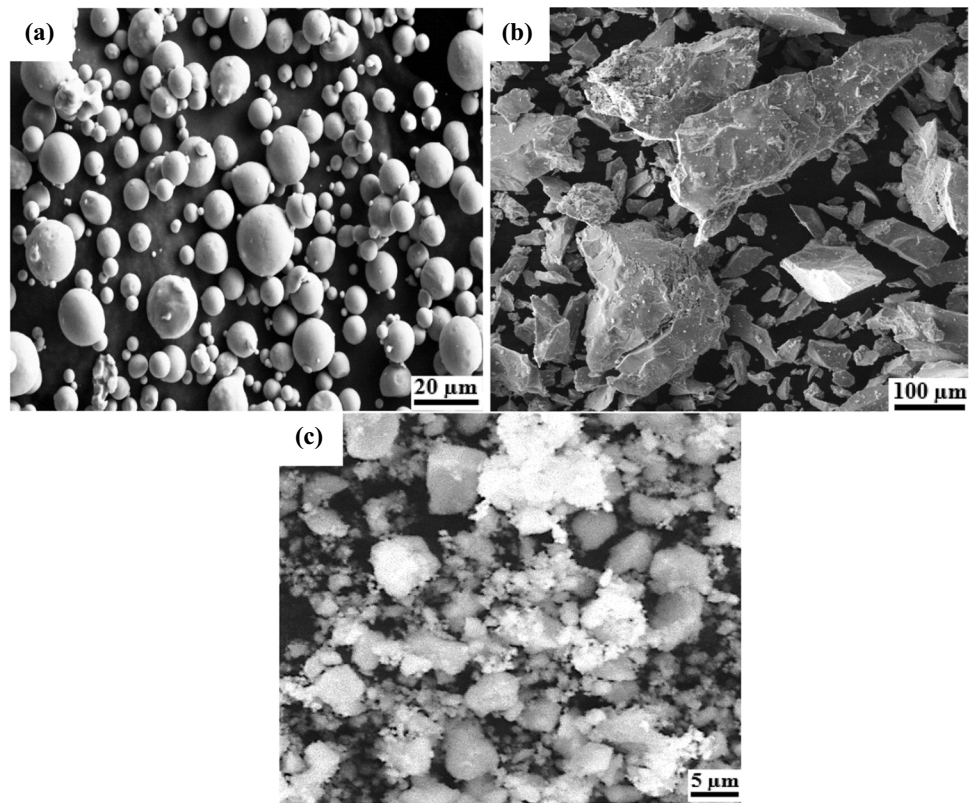**Table 1** Sample composition and identification

Sample	Identification
Pure aluminium	Pure Al
Pure Al + 2 vol% TiFe + 2 vol% ZrO_2	Al + 2% TiFe + 2% ZrO_2
Pure Al + 2 vol% TiFe + 5 vol% ZrO_2	Al + 2% TiFe + 5% ZrO_2
Pure Al + 5 vol% TiFe + 2 vol% ZrO_2	Al + 5% TiFe + 2% ZrO_2
Pure Al + 5 vol% TiFe + 5 vol% ZrO_2	Al + 5% TiFe + 5% ZrO_2

and 40 kV, operating at a continuous scan mode. The surfaces of the samples were prepared using standard metallographic procedures. This was done by grinding from 200 to 1200 grits of silicon carbide emery paper and polished using 9, 6, and 3 µ diamond suspension on different polishing clothes until a shiny surface was clear enough for microstructural analysis obtained. To ensure complete removal of the polishing suspensions, the surface of the specimens was cleaned with acetone. A Zeiss optical microscope and Zeiss Ultra field emission scanning electron microscope (FE-SEM) were used to investigate the morphology of the specimens. The Vickers hardness measurement was taken using an Innovatest Falcon 507 hardness tester across the surface of the specimen, as observed under the microscopes attached to the equipment. A 10 g load was applied, and the final hardness value was obtained from the average of 10 indentations taken across the reinforcement and matrix phases. The frictional coefficient of the samples was determined using a ball-on-disc Anton Paar tribometer, which operates in a dry condition. A zirconia ball with a surface roughness of 20 nm was used as the counterface material, while an applied load and a linear speed of 7 N and 9.5 cm/s were maintained throughout the test. The morphology of the worn surface was examined under FE-SEM for a better understanding on the mode of wear/deformation that took place during the sliding of the counteface ball over the surface of the samples. Nanomechanical analyses were conducted on the specimens using a CSM nanoindenter machine. The surface of the specimens was indented by a Beckovich precision diamond indenter attached to the equipment after the metallographic examination. The loading and unloading rates were fixed at 50 mN, while a pause time of 20 s was maintained all through the test. Nanomechanical properties such as nanohardness and elastic modulus were determined from the loading and unloading curves according to Oliver and Pharr procedure by fitting the data from the unloading portion according to the power-law equation [25] shown in Eq. 1.

$$P = \alpha \left(h - h_k \right)^d \qquad (1)$$

where P is the power law, α and d are the fitting parameters, and h and h_k are the initial and final depth after loading and unloading.

3 Results and discussion

3.1 Phase analysis

The phase identification of peaks as analysed by X'pert HighScore software is shown in Fig. 2. The addition of the reinforcement particles resulted in a positive shift, and this behaviour can be ascribed to the change in the initial particle size of the pure aluminium matrix. The peak shift could also be attributed to increased binding energy owing to the incorporation of the reinforcement particles, thereby enhancing mechanical properties through increased binding energy. The formation of new phases such as Al_3Zr, Fe_2Ti, Al_2TiO_3, $TiZr_3$, and many more is evident from the analysis conducted. The formation of these compounds is based on the interfacial reaction, which was supported by mechanical turbula mixing and compaction at a sufficient temperature, high enough to melt the aluminium matrix, and promote adequate atomic diffusion between the matrix and reinforcement particles. Furthermore, the change in peak morphology of all the composites indicates the exhibition of a second metastable aluminium phase upon the addition of the TiFe and ZrO_2 reinforcements. This behaviour can be ascribed to adequate compaction of the powders, leading to lattice distortion of the parent aluminium crystals. The crystal lattice distortion $(\varepsilon^2)^{1/2}$ of the major peaks with $5\%ZrO_2+2\%TiFe$

and $2\%ZrO_2+5\%TiFe$ is almost double compared with the pure aluminium specimen, indicating a high degree of microstrain within the crystal. The crystallite size and lattice strain of the sintered compacts are evaluated according to the Williamson-Hall approach stated in Eq. 2 [26], and the values obtained are presented in Table 2. The pure aluminium specimen recorded the highest crystallite size of 36.5 nm, while the least crystallite size of 20.84 nm is seen in the composite reinforced with $2\%TiFe+2\%ZrO_2$. The reduction observed in the crystal sizes of the composites evident in the composite could be as a result of rapid heating

Table 2 Crystallite size and lattice strain for sintered pure aluminium and composites

Specimen	Crystallite size (nm)	Lattice strain (%)	Space group
Pure Al	36.50	0.094	200: Pm-3
Al + 2% TiFe + 2% ZrO₂	20.84	0.127	225: Fm-3m
Al + 2% TiFe + 5% ZrO₂	26.14	0.147	227: Fd-3m
Al + 5% TiFe + 2% ZrO₂	33.69	0.101	221: Pm-3m
Al + 5% TiFe + 5% ZrO₂	27.41	0.099	139: I4/mmm

Fig. 2 XRD phase analysis of sintered compacts
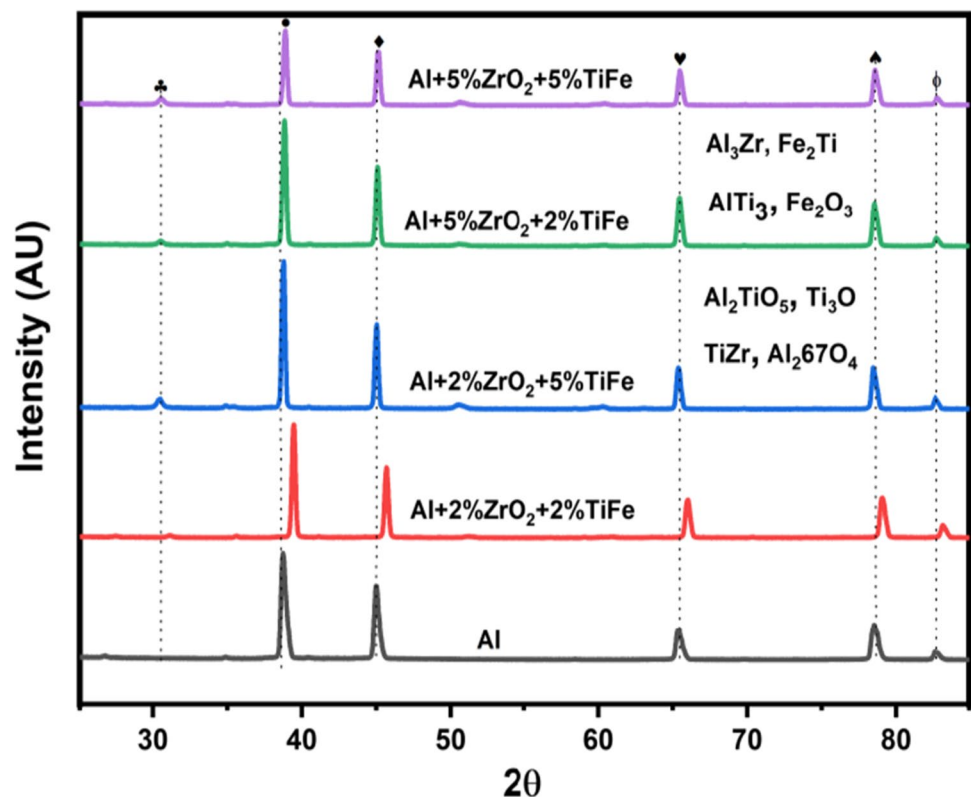
and cooling of the samples during the sintering fabrication process. During recrystallization, new crystals grow around the reinforcement particles, which settle at the grain boundary [27]. Also, all the composites exhibited increased lattice strain, which is a measure of lattice dislocation formed from crystal imperfections [28]. Notably, a rapid increase in lattice strain could result in the formation of brittle surfaces owing to the extreme refinement of the crystals [29]. The space group, which is the combination of translational symmetry exhibited by each unit cell contained in the aluminium composites, is also included in Table 3.

$$\beta \, \cos \, \theta = \frac{J\lambda}{G} + 4 \, \sigma \, sin \, \theta \qquad (2)$$

where β is the full-width half maximum of diffracted peaks, J is the Scherrer constant, λ is the X-ray wavelength, G is the grain size, σ is the internal strain, and θ is the Bragg angle.

3.2 Microstructural characterization

The micrographs of the as-cast composites as observed under an optical microscope are presented in Fig. 3a-d. The micrograph of the pure aluminium seen in Fig. 3a reveals the formation of equiaxed grains. However, the incorporation of reinforcement particles led to the distortion of this morphology, as the grains become irregularly shaped, as evident in Fig. 3b and c. Further observation of Fig. 3d and e also reveals black and grey spots, representing the dispersed ferrotitanium and zirconia reinforcement particles. It is evident that the turbula mixing and spark plasma sintering techniques adopted for the production of the aluminium composite promoted a homogeneous dispersion of the reinforcement particles and adequate bonding between the reinforcement particles and aluminium matrix [30]. Moreover, previous studies on the fabrication of aluminium-based composites have shown that the proper distribution of reinforcement particles often promotes grain refinement, resulting in improved mechanical properties [31, 32]. The SEM micrographs of the specimens are also shown in Fig. 4, and it validates the images obtained from the optical microscope as it shows the arrangement of grains. Figure 4a, which shows the micrograph of pure aluminium reveals several grain boundaries present within the aluminium matrix.

Commercially pure aluminium always contains impurity elements such as iron and silicon, however, the solubility of the elements is almost negligible. This makes the phases of the Al-Fe-Si or Al-Fe interfaces refined in the microstructure. Owing to the rapid solidification and cooling of the spark plasma sintering process, a number of metastable non-equilibrium phases are also formed. From Fig. 4b and c, grain growth is not observed, despite the sintering process being conducted at a temperature sufficient to facilitate grain growth in aluminium-based composites. At the same time, the grain growth hindrance mechanism exhibited by these composites can result from the pinning effect of the TiFe and ZrO_2 particles. The continuous heating cycle and applied pressure from the sintering process have also been proven to be effective in promoting grain size reduction [33, 34]. The grain boundaries of composites shown in Fig. 4d and e are seen to have a black and white outline, respectively, indicating the reinforcement settling across the grain boundaries. The absence of pores in the microstructure confirms high densification of the sintered compacts, which likely resulted from excellent bonding between the reinforcement particles and the aluminium matrix [35]. It is also important to note that the smaller inter-dendritic structures seen in the microstructures are as a result of the fast cooling of the composite during the fabrication process [36, 37].

3.3 Hardness test

Hardness testing is carried out to evaluate the strength of the material through the resistance it offers to an externally applied load. The plot illustrated in Fig. 5 describes the hardness values recorded by pure aluminium and reinforced composites. Sintering at a relatively high temperature ensures adequate bonding between the matrix and reinforcement particles without grain growth, thereby leading to a larger interfacial area within the fabricated composites. The sample with 5% TiFe and 5% ZrO_2 reinforcement particles recorded the highest hardness value of 69.07 HV, while the least hardness property was exhibited by pure aluminium, which records a value of 26.1 HV. Further observation shows that the incorporation of reinforcement particles is seen to positively influence the hardness property of the composites. The increased hardness value seen in the specimen reinforced

Table 3 Nanomechanical properties of pure aluminium and reinforced composites

Sample	Penetration depth (nm)	Reduced Elastic modulus (GPa)	Indentation creep (%)	H/Er (GPa)
Pure Al	1229.42	61.98	2.44	0.0045
Al + 2% TiFe + 2% ZrO_2	797	75.13	2.58	0.0089
Al + 2% TiFe + 5% ZrO_2	880.58	85.45	2.94	0.0067
Al + 5% TiFe + 2% ZrO_2	807.49	89.84	2.62	0.0072
Al + 5% TiFe + 5% ZrO_2	752.48	82.44	2.65	0.0091

(a)

Equiaxed Al grains

20 μm

(b)

TiFe

Al grains

ZrO$_2$

20 μm

(c)

ZrO$_2$

TiFe

20 μm

(d)

ZrO$_2$

20 μm

(e)

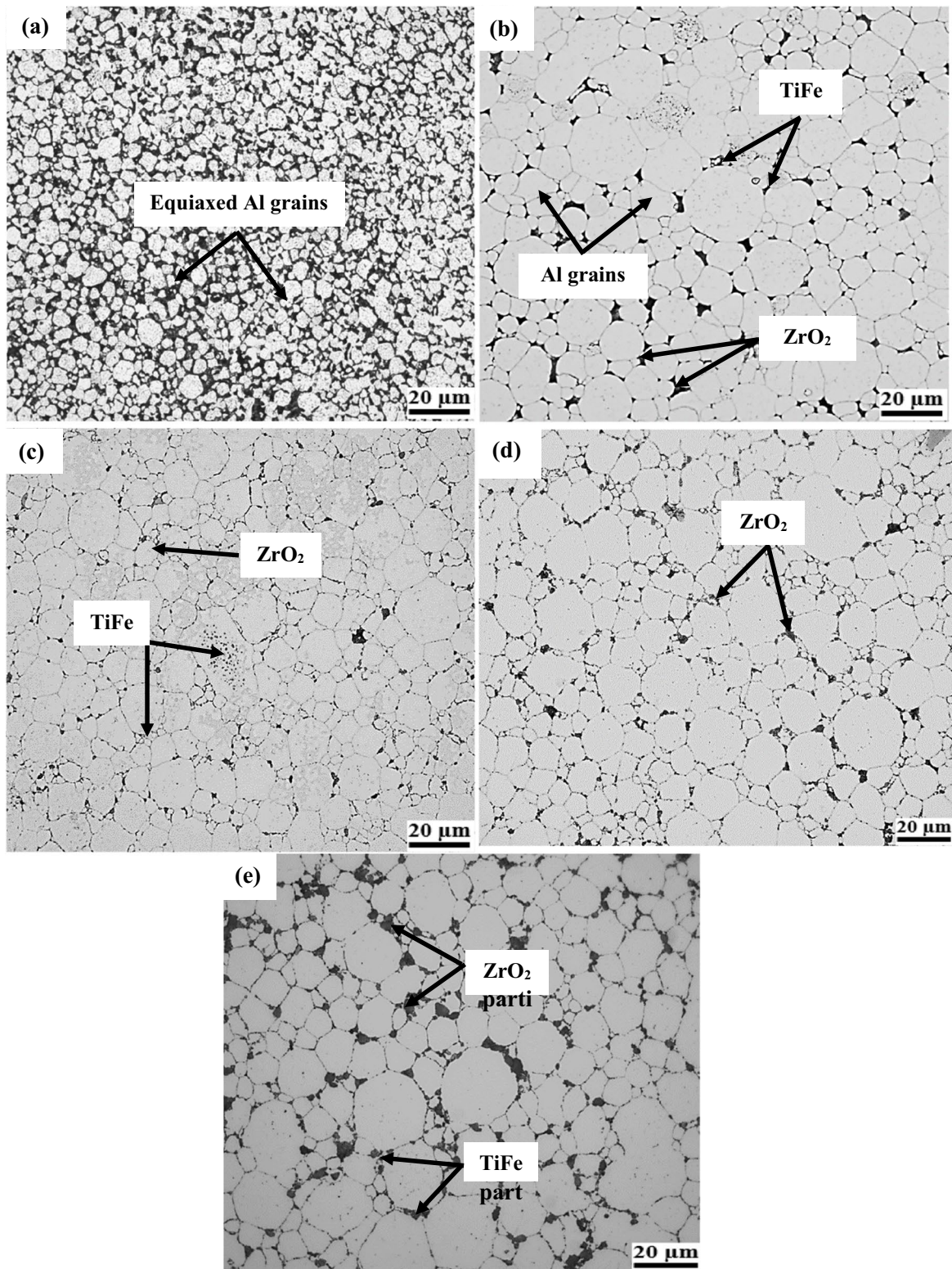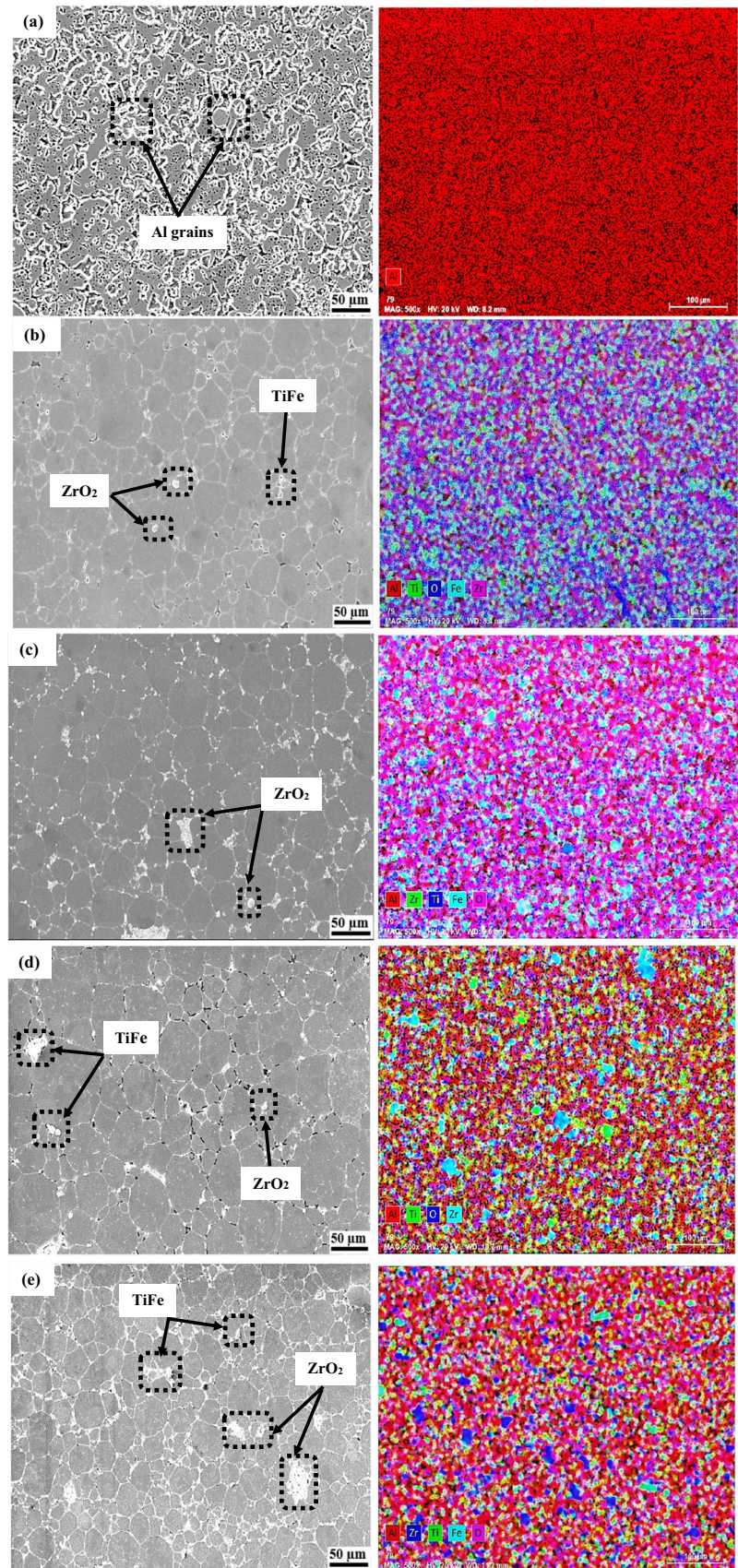ZrO$_2$
parti

TiFe
part

20 μm

Fig. 3 **A** Pure Al. **b** Al + 2% TiFe + 2% ZrO$_2$. **c** Al + 5% TiFe + 2% ZrO$_2$. **d** Al + 2% TiFe + 5% ZrO$_2$. **e** Al + 5% TiFe + 5% ZrO$_2$
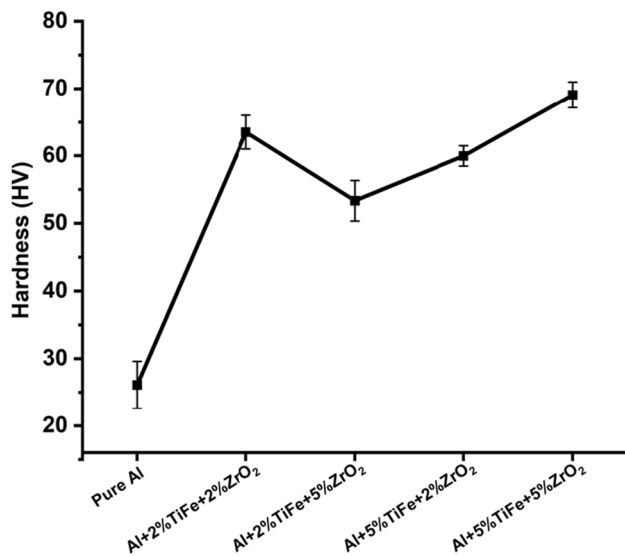
Fig. 4 SEM and EDS mapping of sintered **a** Pure Al, **b** Al + 2% TiFe + 2% ZrO_2, **c** Al + 5% TiFe + 2% ZrO_2, **d** Al + 2% TiFe + 5% ZrO_2, and **e** Al + 5% TiFe + 5% ZrO_2

Fig. 5 Vickers hardness plot of pure aluminium and composites

with the combination of 5% TiFe and 5% ZrO$_2$ can be attributed to microstructural refinement, which was facilitated by the reinforcement particles. Furthermore, the presence of these particles opposes free dislocation movement upon the application of external load. A similar observation was reported in a study by Akinwamide et al. [38]. According to a study by Rice et al. [39], hardness value increases with decreasing grain size according to Eq. 3 as described by

Hall-Petch strengthening. This mechanism describes the relationship between grain size and the strength of a material. A grain size reduction can inhibit easy dislocation movement, thereby increasing the hardness of the composites [40]. The grain boundaries hinder dislocation movement since the high boundary energy of incoherent grain boundaries provides a strong barrier for dislocation transmission from one grain to another [41]. It should also be noted that additional reduction of grain sizes to a range of 12–30 nm can result in failure of the Hall-Petch relationship [42].

$$HV \; \alpha \; G^{-\frac{1}{2}} \tag{3}$$

where HV is the hardness value and G is the grain size.

3.4 Frictional coefficient

The role of friction in engineering materials is significant, as it provides the response of the material to deformation during the wear process [43]. The coefficient of friction can be defined as the ratio between the tangential and normal forces. The plot of the frictional coefficient exhibited by the specimens at room temperature is presented in Fig. 6. Fluctuations are seen to be dominant from the beginning to the end of the test in the reinforced composites. This behaviour can be ascribed to continuous gliding of the alumina counterface material over the reinforcement particles contained in the specimen, and also to the forceful removal of the reinforcement particles from

Fig. 6 Frictional coefficient plot of pure aluminium and composites
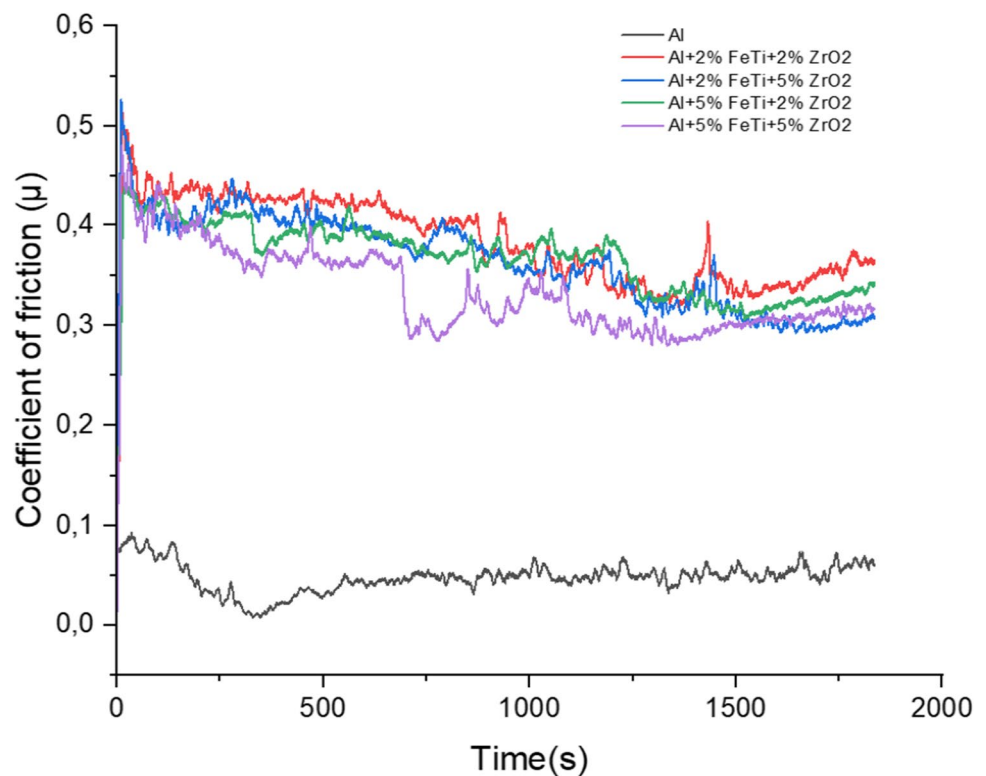
the surface of the composites. Further observation reveals that the pure aluminium exhibited a reduced frictional coefficient owing to reduced heat generated between the alumina ball and the specimen [44]. This further indicates that the counterface ball could glide over the pure aluminium surface without resistance, thereby promoting the formation of an oxide layer on the surface of the specimen, which reduces heat generation [45]. The TiFe and ZrO$_2$ reinforced composites are seen to exhibit an increased heat generation, hence, recording a higher frictional coefficient. The presence of reinforcement particles has been reported to subject aluminium composites to abrasive wear due to the brittleness and hardness induced by the particles [46, 47]. Conclusively, the frictional coefficient is significantly enhanced due to the ineffectiveness of dislocations in the alloy, which increases the hardness and wear resistance of the composites [48]. The SEM morphology of the wear tracks is presented in Fig. 7a-e. It could be seen that during sliding, the formation of grooves [49] is evident in Fig. 7a. This behaviour can be attributed to the presence of ploughing of the pure aluminium specimen by the zirconia counterface material. From Fig. 7b, the incorporation of reinforcement particles increases the hardness strength of the specimen, thereby leading to adhesive wear, which is the removal of material from a less resistant surface during wear. Spalling wear process seen in Fig. 7c results from the repeated sliding between the counterface and specimen surface, leading to surface fatigue. Simsek et al. [50] reported a similar observation on zirconia reinforced aluminium matrix composites in their investigation. Figure 7d and e show the presence of delamination wear from surface resistant to plastic deformation offered by the reinforcement particles [51].

3.5 Nanoindentation properties

The nanoindentation tests were performed by maintaining an equidistance load indentation along a line which cuts across the matrix and reinforcement phases, as shown in Fig. 8. An indentation spacing of 5 μm was maintained throughout the test to prevent work hardening effect. Figure 9 illustrates the load-displacement curves for the pure aluminium and reinforced composites, which exhibit different loading and unloading curves. The loading curve for the pure aluminium demonstrates a reduced slope, which confirms the free movement of dislocations induced by the diamond indenter. However, all the reinforced composites are seen to exhibit a similar slope during the initial loading. This behaviour can be ascribed to a rapid impediment to dislocation movement in the loading direction [52]. Further observation shows the absence of pinning effect in the loading curves due to even distribution of the reinforcements within the aluminium matrix. The unloading part of the curve, which represents the response of the specimens to elastic recovery owing

to a change in residual indentation depth, is similar for all the sintered compacts. The obtained nanohardness values with error bars for the samples are shown in Fig. 10. The specimen which contains 5%TiFe+5%ZrO2 records the highest nanohardness value of 745.81 MPa. In comparison, the pure aluminium sample shows the least nanohardness value of 281.92 MPa. Further observation reveals that the pure aluminium sample reinforced with 2%TiFe+2%ZrO$_2$ also showed improved nanohardness as it presents a value of 676.96 MPa, which is 14.9% and 4.4% higher than the values recorded by the sample reinforced with 2%TiFe+5%ZrO$_2$ and 5%TiFe+2%ZrO$_2$ respectively. The improved nanohardness shown by the composites confirms the stiffening and strengthening effect of the ZrO$_2$ and TiFe reinforcements in the aluminium matrix [53]. A study by Antillon et al. [54] has shown that the combined Voigt-Reuss model helps predict the stiffening effect of randomly dispersed reinforcements according to Eq. 4. It is also noteworthy that the continuous model does not account for porosities and is based on a simple rule of mixture (ROM).

$$E = \frac{3}{8}E_a + \frac{5}{8}E_b \tag{4}$$

where E is the modulus of elasticity and subscripts a and b are the Voigt and Reuss condition. E_a and E_b are estimated according to Eqs. 5 and 6 respectively.

$$E_a = kV_pE_p + \left(1 - V_p\right)E_f \tag{5}$$

$$E_b = \frac{(Ep)^2}{E_p\left(1 - V_p\right) + E_fV_p} \tag{6}$$

where V is the volume fraction, k is the load transfer efficiency ($\approx \frac{1}{5}$), and subscripts f and p are the properties of matrix and reinforcements respectively.

Other nanomechanical properties, such as penetration depth, reduced elastic modulus, indentation creep and work of indentation, are presented in Table 3. The decreased penetration depth displayed by the composites confirms adequate bonding between the matrix and reinforcement particles. In addition, the reduced elastic modulus is seen to be significantly enhanced upon the incorporation of ZrO$_2$ and TiFe reinforcements. This property is dependent on forces that coexist between the crystal morphology and atomic bond of the present phases. This enhancement can also be ascribed to the formation of secondary phases resulting from the interaction between the aluminium matrix and reinforcement phases [55]. The indentation creep is the relative change in indentation depth at constant load and is seen to be higher in the reinforced samples, as the least indentation creep of 2.4% is recorded in the unreinforced aluminium sample.
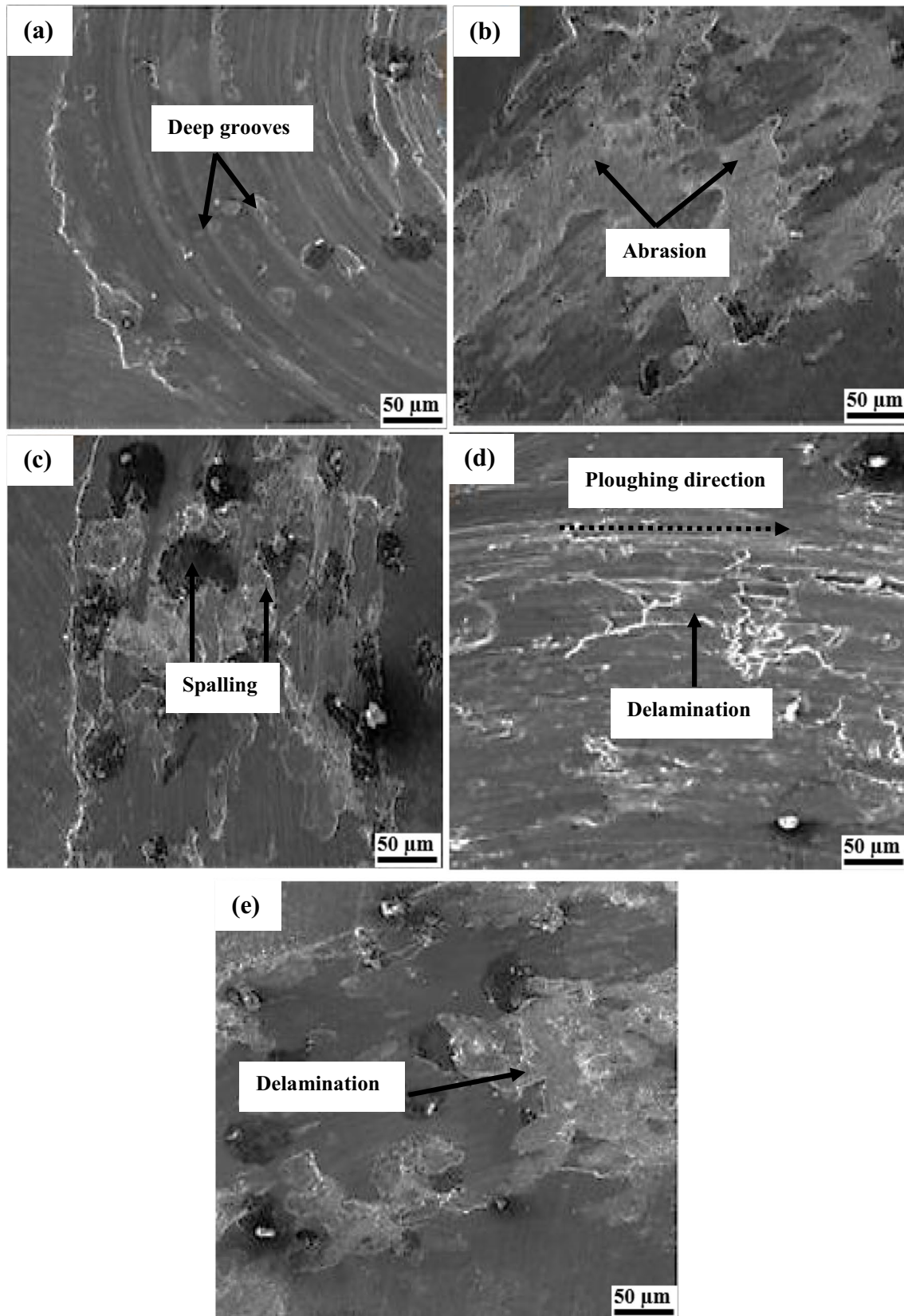
Fig. 7 SEM morphology of worn tracks of **a** pure Al, **b** Al + 2% TiFe + 2% ZrO$_2$, **c** Al + 5% TiFe + 2% ZrO$_2$, **d** Al + 2% TiFe + 5% ZrO$_2$, and **e** Al + 5% TiFe + 5% ZrO$_2$
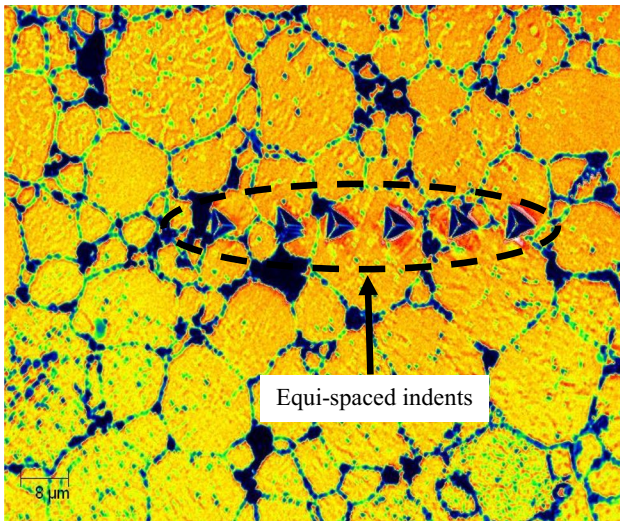
Fig. 8 Micrograph of indentation profile of Berkovich indenter across matrix and reinforcement phases during nanoindentation testing

- The turbular mixing of the powders promoted the homogeneous distribution of ZrO_2 and TiFe powders within the aluminium matrix. This was further confirmed by the presence of new phases such as Fe_2Ti and $TiZr_3$ from the XRD phase analysis of the sintered composites.
- The Williamson-Hall method was used for determining the grain size and lattice strain, and it confirmed that a high level of microstrain exists within the crystals of the composites.
- The absence of visible pores in the optical and SEM micrographs confirmed high densification and adequate compaction between the matrix and reinforcement particles, which in turn confirms the effectiveness of the spark plasma sintering technique adopted for fabrication.
- Mechanical and nanomechanical tests also showed that the composites were strengthened via the load-transfer mechanism, as they all exhibited improved hardness, enhanced tribological behaviour, and increased modulus of elasticity.

4 Conclusion

This microstructural and mechanical characterization of hybrid aluminium-based composites fabricated via spark plasma sintering was investigated from this study; and the following scientific conclusions were drawn:

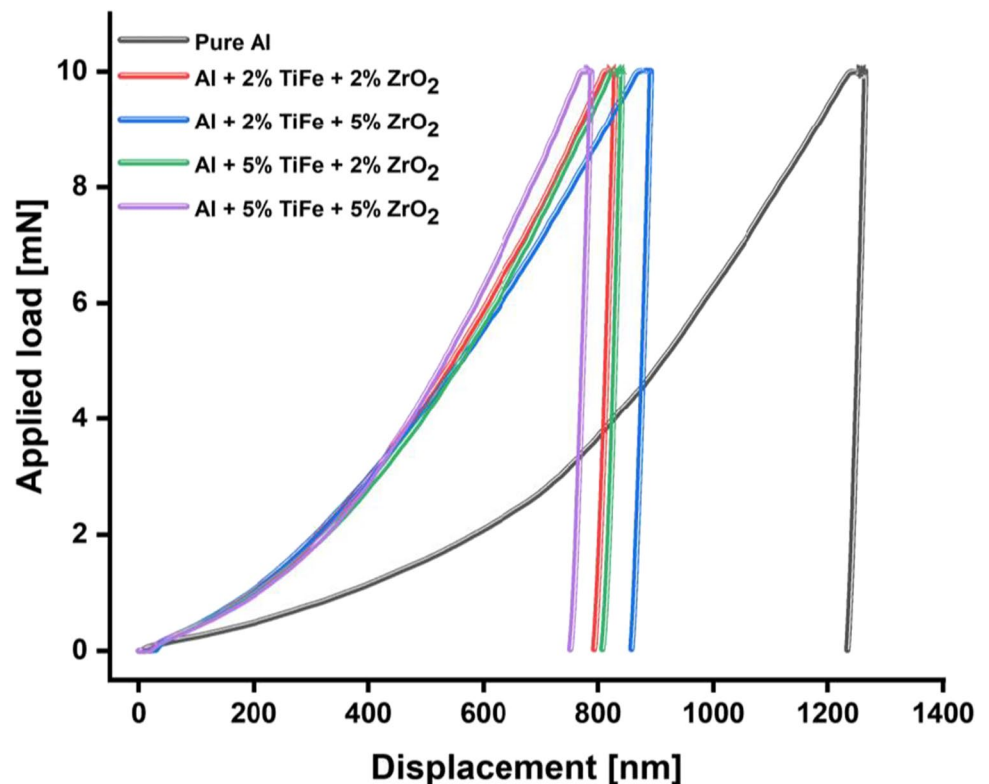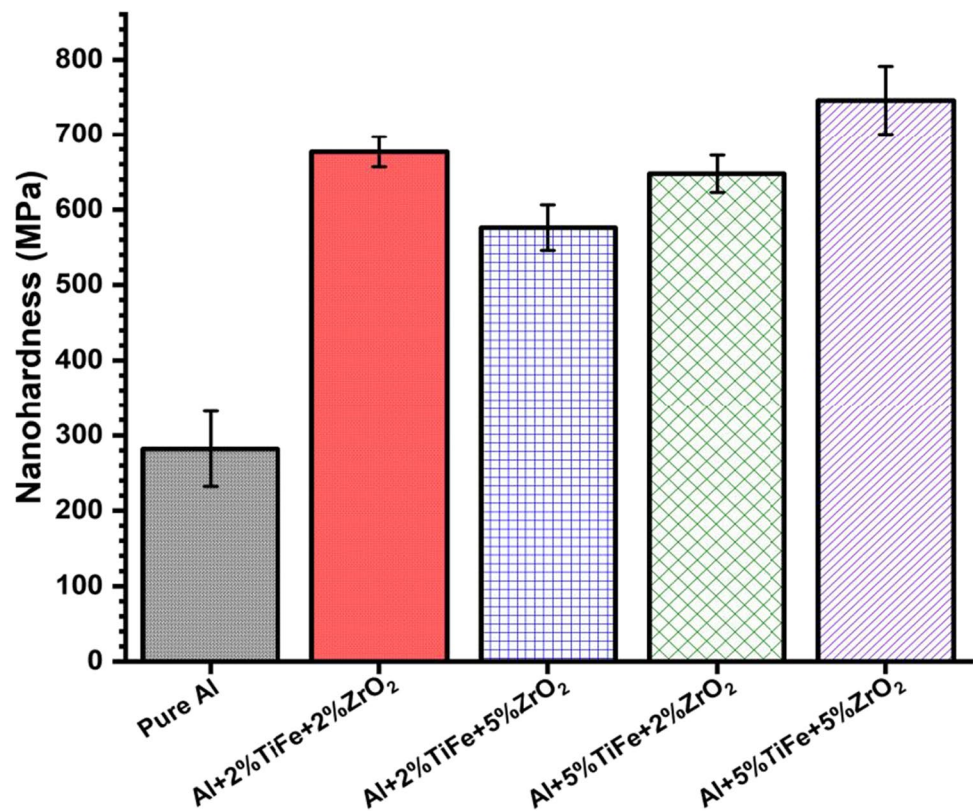**Fig. 9** Applied load-displacement curves for sintered compacts

Fig. 10 Plot of nanohardness
with error bars for sintered
compacts

Declarations

Conflict of interest The authors declare no competing interests.

References

1. Saravanan C, et al (2020) *Assessment of mechanical properties of Silicon Carbide and Graphene reinforced aluminium composite.* Materials Today Proceeding, 2020

2. Owoputi AO, Inambao FL, Ebhota WS (2020) Effect of percentage weight and particle size of SiCp reinforcement on the mechanical behaviour of functionally graded aluminum metal matrix. Int J Eng Res Technol 13(3):444–453

3. Akinwamide S.O et al (2020) *Characterization of microstructure, mechanical properties and corrosion response of aluminium-based composites fabricated via casting—a review.* The International Journal of Advanced Manufacturing Technology, 2020: p. 1-17

4. Akinwamide S.O et al (2019) *A nanoindentation study on Al (TiFe-Mg-SiC) composites fabricated via stir casting.* in *Key Engineering Materials.* 2019. Trans Tech Publ

5. Owoputi AO, Inambao FL, Ebhota WS (2018) A review of functionally graded materials: fabrication processes and applications. Int J Appl Eng Res 13(23):16141–16151

6. Faisal N, Kumar K (2018) Mechanical and tribological behaviour of nano scaled silicon carbide reinforced aluminium composites. J Exp Nanosci 13(sup1):S1–S13

7. Owoputi AO, Inambao F, Ebhota W (2019) Influence of SiCp Reinforcement on the Mechanical Properties of Functionally Graded Aluminum Metal Matrix Composites Fabricated by Centrifugal Casting Technique. Int J Mechanical Eng Technol 10(8):306–316

8. Srivastava A et al (2014) A review on fabrication & characterization of hybrid aluminium metal matrix composite. Int J Adv Res Innovat 1(2):242–246

9. Jeevanantham V, Vadivelu P, Manigandan P (2017) Material based structural analysis of a typical landing gear. Int J Innovat Sci, Eng Technol 4(4):295–300

10. Surappa MK (2003) Aluminium matrix composites: Challenges and opportunities. Sadhana 28(1):319–334

11. Green D.J., Hannink RH, Swain MV (2018) *Transformation toughening of ceramics.* 2018: CRC press

12. Weigelt C et al (2017) Compressive and tensile deformation behaviour of TRIP steel-matrix composite materials with reinforcing additions of zirconia and/or aluminium titanate. J Alloys Compounds 695:9–20

13. Naik G et al (2017) *Experimental Investigations on Dry Sliding Wear Behaviour of Aluminium 6061 Metal Matrix Composite.* 2017. 5

14. Gecu R, Karaaslan A (2019) A comparative study on titanium-reinforced aluminium matrix composites produced by melt infiltration casting and squeeze infiltration. Int J Metalcasting 13(2):311–319

15. Akinwamide SO et al (2020) Influence of heat treatment on microstructural and mechanical behavior of stir cast Al-(TiFe-SiC) composites. Mater Today: Proceed 28:725–729

16. Scudino S et al (2009) Powder metallurgy of Al-based metal matrix composites reinforced with β-Al3Mg2 intermetallic particles: Analysis and modeling of mechanical properties. Acta Materialia 57(15):4529–4538

17. Mekgwe GN et al (2021) Fabrication of graphite reinforced TiCxNy by spark plasma sintering technique: A comparative assessment of microstructural integrity and nanoindentation properties. Vacuum 187:110144

18. Chu K et al (2010) Thermal conductivity of spark plasma sintering consolidated SiCp/Al composites containing pores: Numerical study and experimental validation. Composites Part A: Appl Sci Manuf 41(1):161–167

19. Msweli NP et al (2023) Microstructure and biocorrosion studies of spark plasma sintered yttria stabilized zirconia reinforced Ti6Al7Nb alloy in Hanks' solution. Mater Chem Phys 293:126940

20. Akinwamide SO et al (2019) Characterization and mechanical response of novel Al-(Mg–TiFe–SiC) metal matrix composites developed by stir casting technique. J Composite Mater 53(28–30):3929–3938

21. Jimınez S, Lima R, Castaρo V (1999) Synthesis of an aluminium-zirconia composite through powder metallurgy and sol-gel. Adv Composites Lett 8(4):096369359900800403

22. Kuldeep B et al (2018) Effect of boron nitride and zirconium dioxide on mechanical behavior of Al7075 metal matrix hybrid composite. Mater Res Exp 6(3):036509

23. Suresha S, Sridhara B (2010) Wear characteristics of hybrid aluminium matrix composites reinforced with graphite and silicon carbide particulates. Composites Sci Technol 70(11):1652–1659

24. James SJ et al (2014) Hybrid aluminium metal matrix composite reinforced with SiC and TiB2. Procedia Eng 97:1018–1026

25. Oliver WC, Pharr GM (1992) An improved technique for determining hardness and elastic modulus using load and displacement sensing indentation experiments. J Mater Res 7(6):1564–1583

26. Devesa S et al (2021) Williamson-hall analysis in estimation of crystallite size and lattice strain in Bi1 34Fe0 66Nb1 34O6 35 prepared by the sol-gel method. Mater Sci Eng: B 263:114830

27. Sahoo B et al (2019) Particle size and shape effects on the surface mechanical properties of aluminium coated with carbonaceous materials. J Composite Mater 53(2):261–270

28. Mishra S et al (2015) *A comparative assessment of crystallite size and lattice strain in differently cast A356 aluminium alloy.* in *IOP Conference Series: Materials Science and Engineering.* 2015. IOP Publishing

29. Seikh AH et al (2019) Microstructural and corrosion characteristics of Al-Fe alloys produced by high-frequency induction-sintering process. Coatings 9(10):686

30. Akash R et al (2021) Synthesis and testing of aluminium composite using industrial waste as reinforcement. Mater Today: Proceed 37:634–637

31. Al-maamari AEA, Iqbal AA, Nuruzzaman DM (2019) Wear and mechanical characterization of Mg–Gr self-lubricating composite fabricated by mechanical alloying. J Magnesium Alloys 7(2):283–290

32. Zamani NABN, Iqbal AA, Nuruzzaman DM (2019) Mechanical and tribological behavior of powder metallurgy processed aluminum–graphite composite. Russian J Non-Ferrous Metals 60(3):274–281

33. Zamora V et al (2012) Crystal-size dependence of the spark-plasma-sintering kinetics of ZrB2 ultra-high-temperature ceramics. J Eur Ceramic Soc 32(2):271–276

34. Cha SI, Hong SH (2003) Microstructures of binderless tungsten carbides sintered by spark plasma sintering process. Mater Sci Eng: A 356(1–2):381–389

35. Nassar AE, Nassar EE (2017) Properties of aluminum matrix Nano composites prepared by powder metallurgy processing. J King Saud University-Eng Sci 29(3):295–299

36. Asgharzadeh H, Simchi A (2009) Supersolidus liquid phase sintering of Al6061/SiC metal matrix composites. Powder Metallurgy 52(1):28–35

37. Aravind M et al (2004) Formation of Al2Cu and AlCu intermetallics in Al (Cu) alloy matrix composites by reaction sintering. Mater Sci Eng: A 380(1–2):384–393

38. Akinwamide SO, Akinribide OJ, Olubambi PA (2021) Microstructural evolution, mechanical and nanoindentation studies of stir cast binary and ternary aluminium based composites. J Alloys Compounds 850:156586

39. Rice RW, Wu CC, Boichelt F (1994) Hardness–grain-size relations in ceramics. J Am Ceramic Soc 77(10):2539–2553

40. Krell A, Blank P (1995) Grain size dependence of hardness in dense submicrometer alumina. J Am Ceramic Soc 78(4):1118–1120

41. Lu K (2016) Stabilizing nanostructures in metals using grain and twin boundary architectures. Nat Rev Mater 1(5):1–13

42. Wu H, Fan G (2020) An overview of tailoring strain delocalization for strength-ductility synergy. Progress Mater Sci 113:100675

43. Zhang C, Feng P, Zhang J (2013) Ultrasonic vibration-assisted scratch-induced characteristics of C-plane sapphire with a spherical indenter. Int J Machine Tools Manuf 64:38–48

44. Sharma VK, Singh RC, Chaudhary R (2017) Effect of flyash particles with aluminium melt on the wear of aluminium metal matrix composites. Eng Sci Technol, Int J 20(4):1318–1323

45. Koltsova T et al (2018) Operational characteristics of the composite aluminum-carbon nanofibers. Mater Phys Mechanics 38(1):11–15

46. Yılmaz O, Buytoz S (2001) Abrasive wear of Al2O3-reinforced aluminium-based MMCs. Composites Sci Technol 61(16):2381–2392

47. Zhang Z, Zhang L, Mai Y-W (1995) Particle effects on friction and wear of aluminium matrix composites. J Mater Sci 30(23):5999–6004

48. Mekgwe G.N et al (2022) *Insight into tribological and corrosion behaviour of binderless TiCxNy ceramic composites processed via pulsed electric current sintering technique.* Ceramics International, 2022

49. Anbuchezhiyan G et al (2021) Synthesis and Characterization of Silicon Nitride Reinforced Al–Mg–Zn Alloy Composites. Metals Mater Int 27(8):3058–3069

50. Simsek D et al (2022) Optimizing of Wear Performance on Elevated Temperature of ZrO 2 Reinforced AMCs Using Weighted Superposition Attraction Algorithm. J Sci Industrial Res (JSIR) 81(05):462–474

51. Idusuyi N, Olayinka JI (2019) Dry sliding wear characteristics of aluminium metal matrix composites: a brief overview. J Mater Res Technol 8(3):3338–3346

52. Ram HA, Koppad PG, Kashyap K (2013) Nanoindentation studies on MWCNT/aluminum alloy 6061 nanocomposites. Mater Sci Eng: A 559:920–923

53. Tham L, Gupta M, Cheng L (2001) Effect of limited matrix–reinforcement interfacial reaction on enhancing the mechanical properties of aluminium–silicon carbide composites. Acta Materialia 49(16):3243–3253

54. Antillon M et al (2018) Strengthening in boron nitride nanotube reinforced aluminum composites prepared by roll bonding. Adv Eng Mater 20(8):1800122

55. Shankar G et al (2013) Individual and combined effect of reinforcements on stir cast aluminium metal matrix composites-a review. Int J Curr Eng Technol 3(3):922–934